



Original Research

Application of intravoxel incoherent motion imaging in the study of migration and movement of cancer cells

Yilei Wang¹, Haixiao Xu^{1*}, Idris Jerjes Ahmed²

¹Sports Department, Hangzhou Medical College, Hangzhou, 310053, China

²Radiology Unit, Department of Surgery, Hawler Medical University, Erbil, Kurdistan Region, Iraq

*Correspondence to: xuhaixiao@163.com

Received January 28, 2020; Accepted September 7, 2020; Published October 31, 2020

Doi: <http://dx.doi.org/10.14715/cmb/2020.66.7.21>

Copyright: © 2020 by the C.M.B. Association. All rights reserved.

Abstract: IVIM imaging technology can obtain physiological information of tissue cells and blood perfusion at the same time in one imaging process. Taking female patients in Shenzhen Maternal and Child Health Hospital affiliated to Southern Medical University as an example, the migration and movement of breast cancer cells and hepatocellular carcinoma cells are studied by intravoxel incoherent motion imaging. Apparent diffusion coefficient (ADC), true diffusion coefficient (D), pseudo-diffusion coefficient (D*) and perfusion fraction (f) are measured by the IVIM bi-index model, and statistical analysis is made. The results show that the IVIM bi-index model can truly reflect the diffusion of water molecules in breast mass-like lesions, and reflect the migration and movement of breast cancer cells. Especially D value has important reference significance for the research and diagnosis of breast cancer cells. IVIM bi-index model has limited diagnostic value for the migration and movement of common hepatocellular carcinoma cells, and ADC value may have higher diagnostic efficiency.

Key words: Intravoxel; Incorelated; Motion Imaging; Cancer Cells; Migration; Motion Law.

Introduction

Perfusion is an important physiological function of blood flow to transmit oxygen and nutrients to tissues and cells through the microcirculation network in tissues (1). The quality of blood perfusion in tissues will directly affect the activity of tissues and cells, thus affecting the physiological function of whole tissues or organs (2). The vast majority of human diseases are caused directly or indirectly by abnormal tissue perfusion, such as myocardial infarction, stroke, renal failure, cancer and so on. On the contrary, the occurrence of many diseases can also lead to abnormal tissue perfusion, such as cirrhosis, hemangioma, cancer and so on (3). In the clinic, a series of clinical indicators derived from tissue perfusions, such as perfusion rate and blood flow velocity, have been widely used in the diagnosis and evaluation of diseases. In addition, tissue perfusion can also be used to evaluate the effect of surgery and the recovery of patients after surgery, because there are obvious differences in blood perfusion before and after some diseases, such as myocardial perfusion rate before and after coronary thrombolysis. Therefore, the accurate measurement of tissue perfusion has important clinical significance for early detection of disease, accurate evaluation of disease condition and post-operative evaluation (4).

Medical imaging technology is the main means of detecting tissue perfusion in the clinic, and it has developed rapidly in recent years. At present, the main imaging technologies that can be used for tissue perfusion

measurement include single-photon emission computed tomography (SPECT), positron emission computed tomography (PET), computed tomography (CT), perfusion imaging, contrast-enhanced ultrasound imaging and dynamic enhanced magnetic resonance imaging (5). These imaging techniques obtain perfusion information by measuring the concentration distribution of imaging agents or contrast agents injected into specific tissues or organs in vitro. Strictly speaking, these imaging techniques are invasive detection methods. For patients with renal insufficiency, the invasion of imaging agents or contrast agents can lead to new diseases such as renal fibrosis, which can lead to renal failure in severe cases. In order to remedy the defect of invasive imaging technology in tissue perfusion measurement, endogenous imaging technology emerged as the times require. The most representative technique is arterial spin labeling imaging. This technique is derived from magnetic resonance imaging. Because there is no need to inject imaging agents or contrast agents in vitro, this technique is suitable for all populations and has received extensive attention in clinical medicine and the medical imaging field (6).

Traditional MR imaging techniques mainly depend on the differences of spin proton density, T_1 value, T_2 value or T_2 value of tissues. DWI, unlike traditional MR imaging techniques, mainly depends on the movement of water molecules in tissues. Quantitative analysis of DWI can provide information that conventional MRI cannot provide, ADC measurement can help to distinguish benign from malignant lesions, predict and moni-

tor the efficacy of radiotherapy and chemotherapy on malignant tumors, etc. For biological tissues, the movement of water molecules has two main aspects: one is the diffusion movement of water molecules, i.e. Brownian motion, which is related to the physical characteristics of tissues and can be used to describe the characteristics of tissues (7); secondly, the microcirculation of blood flow in the capillary network, i.e. perfusion (8). In terms of voxel-level, because of the distribution of pseudo-random organs in the capillary network, when diffusion sensitive gradient is applied, blood perfusion can also cause the phase of proton groups in voxels to be irrelevant, resulting in higher ADC values. If only water molecules diffuse in voxels, the ADC values measured should be the same as the diffusion coefficient D (DC), but in vivo ADC values are often higher, which is due to the water molecules diffuse and blood perfusion components of ADC values. Intraventric Incoherent Motion (IVIM) imaging can be used to quantify two motion components in DWI images. IVIM imaging technology breaks through the concept of traditional perfusion imaging technology. It not only does not have the potential threat of external imaging agents to the human body in invasive perfusion imaging but also avoids the situation of the low signal-to-noise ratio of perfusion image caused by insufficient content of internal imaging agents in non-invasive perfusion imaging (9). In this paper, intravoxel incoherent motion imaging is applied to cancer cell research to analyze the migration and movement of breast cancer cells and hepatocellular carcinoma cells (10).

Materials and Methods

The subjects of this study were female patients in Shenzhen Maternal and Child Health Hospital affiliated to Southern Medical University. The detailed settings are as follows.

Research Method of Breast Cancer Cell Migration and Movement-based on Intravoxel Incoherent Motion Imaging

Research Data

A retrospective analysis was made of 74 patients with mass-like lesions in Shenzhen Maternal and Child Health Hospital affiliated to Southern Medical University from January 2018 to January 2019. The age ranges from 22 to 72 years old, with an average age of (4.31 ± 7.6) years old. Routine MR examination, single- b value and multi- b value DWI were performed two weeks before operation (11). All patients underwent surgical treatment, among which 48 cases were malignant lesions (malignant group), including 41 invasive ductal carcinomas, 2 medullary carcinomas, 3 mucinous adenocarcinomas, 1 ductal carcinoma in situ, and 1 intraductal papillary carcinoma; 26 benign lesions (benign group), including 19 fibroadenomas, 2 giant fibroadenomas, 3 benign phyllodes tumors and 2 intraductal papillomae. Nineteen healthy persons aged 28–43 years old (average (35.9 ± 4.2)) were selected as the control group during the same period. All subjects signed informed consent (12). Based on this setting, the migration and movement of breast cancer cells (lesions) were studied.

Instruments and Methods

Philips Achieva 1.5 TMR scanner and 4-channel phase-controlled coil for breast were used (13). In the prone position, bilateral mammary glands naturally hang in the coil and head-foot position enters the main magnetic field. Two breast axes TSE T1W1, T2W1 and T2W1 fat suppression sequence and sagittal TSE T1W1 fat suppression sequence were made volume scanning, with a thickness of 4 mm. Dynamic enhanced scanning was performed with a 3D THRIVE sequence, and Gd-DTPA was a contrast agent, with a concentration of 0.1 mmol/kg. NEMOTO high-pressure syringe and elbow vein injection at a rate of 2.0 ml/s was used. 10 ml saline was injected intravenously after bolus injection of contrast agent. Firstly, the mask was scanned, the contrast agent was injected at the same time, and the dynamic enhancement scanning was performed for 7 consecutive times (14). Subtraction was performed after scanning. Single b -value DWI uses a single-shot spin plane echo sequence, and diffusion factor b values were $0, 800 \text{ s/mm}^2$. Multi- b -value DWI uses single-shot echo planner images (SS-EPI) and parallel acquisition space-sensitive coding technology (SENSE), with b values of 0, 5, 10, 20, 50, 100, 200, 400, 800, 1200, 2000 s/mm^2 , respectively.

Routine scan sequence and specific parameters of MRI were as:

Axis TSE-T1WI: TR = 500 ms, TE = 11 ms, thickness = 8 mm, interlayer spacing = 0 mm, FOV = 240 mm×240 mm, matrix = 179×256, and excitation number is once;

Axis TSE-T2WI: TR = 2980 ms, TE = 104 ms, thickness = 8 mm, interlayer spacing = 0 mm, FOV = 240 mm×240 mm, matrix = 384×384, and excitation number is twice;

Axis FS-T2WI: TR = 3020 ms, TE = 101 ms, thickness = 8 mm, interlayer spacing = 0 mm, FOV = 240 mm×240 mm, matrix = 320×320, and the excitation number is twice;

Sagittal TSE-T 2WI: TR = 6070 ms, TE = 104 ms, thickness = 5 mm, spacing = 0 mm, FOV = 240 mm×240 mm, matrix = 346 ×384, and the excitation number is twice.

The principle of IVIM imaging is as:

In human biological tissues, IVIM phenomena include the simple diffusion movement of water molecules and blood perfusion. IVIM imaging can be used to quantify diffusion movement components and blood perfusion components respectively. The attenuation of signal intensity accords with the following equation:

$$ADC = \ln(SI_1 / SI_0) / (b_2 - b_1) \quad [1]$$

b is the dispersion factor, $b = \gamma^2 G^2 \delta^2 (\Delta - \delta / \varepsilon)$, the unit is s/mm^2 ; γ is the spin-magnetic ratio; G is the interval time of gradient field; SI_1 and SI_0 are the signal intensity of the corresponding pixels at the same location where the diffusion-sensitive gradient field b_1 is applied and not applied; f is the perfusion fraction; D is the pure diffusion coefficient, representing the diffusion motion of pure water molecules (the slow diffusion motion component), in units of s/mm^2 ; D^* value is a pseudo-diffusion coefficient, which represents the irrelevant

movement of microcirculation in voxels, i.e. perfusion-related diffusion movement, or becomes a component of rapid diffusion movement.

Considering that D^* is significantly larger than D , when b is larger than 200 s/mm^2 , the effect on signal attenuation can be neglected. Equation (1) can be simplified as follows:

$$SI_1 / SI_0 = e^{-bD} \quad [2]$$

At this time, the D value can be obtained by Equation (2). IVIM DWI imaging can be performed by using multiple sets of b values, and the f value and D^* value can be obtained by combining the non-linear fitting algorithm based on Equation (1).

Research Method of Migration and Movement of Hepa Tocellular Carcinoma Cells Based on Intravoxel Incoherent Motion Imaging

Research Materials

A retrospective analysis was made of 60 cases of focal hepatic lesions (FHL) from December 2018 to July 2019 in Shenzhen Maternal and Child Health Hospital affiliated to Southern Medical University. There were 46 elderly women and 14 young women, aged 31-80 years, with an average age of (54.2 ± 11.4) years (15). Among the 60 cases, 17 are hepatic hemangioma and 43 were hepatic malignant lesions, including 30 cases of hepatocellular carcinoma (HCC), 6 cases of intrahepatic cholangiocarcinoma (ICC), 7 cases of hepatic metastasis (each case has multiple lesions, only one of them is selected as representative lesions) (16). In order to set up and study the migration and movement of hepatocellular carcinoma cells (pathological changes), the inclusion criteria were as follows:

Solid FHL, its minimum diameter is D cm;

Pathologically confirmed or imaging findings were typical and confirmed by clinical data and follow-up;

There was no serious artifact in the IVIM bi-index model image (17).

The classical imaging manifestations and follow-up diagnosis of hepatic hemangioma: HCC and ICC are confirmed by operation/puncture records. 5 cases of liver metastases are confirmed by operation/puncture pathology and 2 cases are confirmed by follow-up.

Instruments and Methods

GE Discovery MR 7503.0T MR instrument with an 8-channel body phased-array surface coil was used (18). Before scanning and training, patients were told to fasting for solids and liquids for 4 hours and hold their breath at the end of the breath. The patients were asked to lie on his back, a breath-gating hose is placed, the xiphoid process was located as the center, and the whole liver was scanned. Contrast agent Gd-BOPTA was injected through an elbow vein with a high-pressure syringe at a dose of 0.2 ml/kg body mass and a flow rate of 2 ml/s . Later, 20 ml saline was injected with the same flow rate, and LAVA-FLEX Y1W was used to perform arterial phase, portal phase and delayed phase imaging. The scanning time was 25, 70 and 180 seconds after injection of contrast agent, respectively.

Image Analysis

The ROI of the lesion was determined on DWI images with different b values by dynamic enhanced scanning at the maximum level of the lesion. The mean value was measured three times (the area not less than 9 mm^2) to avoid the liquefied necrosis area as far as possible. In the control group, ROI was measured three times (the area not less than 9 mm^2) to obtain the mean value. Under the platform of METLAB, D value was calculated by using a linear fitting equation. Then the non-linear least-squares method was used to fit and calculate D^* the D^* value and f value of normal tissue, benign tissue and malignant group (19).

Statistical Analysis

PASW Statistics 19.0 software package was used to analyze the data. $P < 0.05$ indicates that the difference is significant. ROC curve was used to determine the best threshold, sensitivity and specificity of each parameter for differential diagnosis of cancer cells. Med Calc 18.2 software was used to compare AUC (20).

Results

Study on Migration and Movement of Breast Cancer Cells Based on Intravoxel Incoherent Motion Imaging

Routine MRI Findings

There were no abnormal signs on conventional MRI. In the benign group, round, oval and lobulated masses with clear margins and low signal segregation were found in 5 lesions. The time-signal curves were type I in 21 cases, type II in 4 cases and type III in 1 case (21). In the malignant group, irregular masses and oval masses were found with unclear margins, clear parts. There were 2 cases of that time-signal curve was the type I, 9 cases of type II, 37 cases of type III, and multi- b value DWI images showed that with the increase of b value, the DWI signal intensity of the lesions decreases gradually (Figure 1).

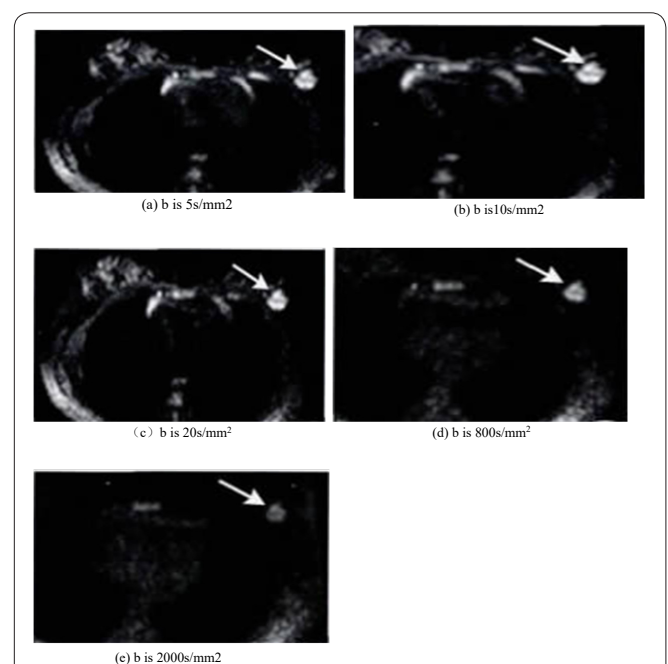


Figure 1. Infiltrating breast cancer, 72 years old. The arrow represents the lesion.

Table 1. Data of 13 groups of subjects.

Group	D ($\times 10^{-3}$ mm ² /s)	f (%)	D ($\times 10^{-3}$ mm ² /s)	ADC ($\times 10^{-3}$ mm ² /s)
Benign group (n=26)	1.30 \pm 0.19	5.80 \pm 2.68	107.24 \pm 17.56	1.34 \pm 0.11
Malignant group (n=48)	0.92 \pm 0.14	9.64 \pm 2.16	90.85 \pm 13.46	1.05 \pm 0.17
Control group (n=19)	1.97 \pm 0.21	4.82 \pm 1.08	127.96 \pm 18.45	1.93 \pm 0.23
F value	272.08	45.98	39.01	167.28
P value	<0.01	<0.01	<0.01	<0.01

DWI Parameters

The data of the three groups are shown in Table 1. There were significant differences in D, f, D* and ADC values between benign and malignant groups (all P < 0.01). The comparison of F-values was based on approximate F-test Welch method with uneven variance, the multiple comparisons were based on Dunnett' the T3 method, the comparison of D, D* and ADC values were based on Fisher test with homogeneity of variance, and the multiple comparisons were based on LSD method (22). The D value of the benign group is lower than that of the control group and higher than that of a malignant group (P < 0.01); the f value of malignant group was higher than that of the control group and benign group (P < 0.01), but there was no significant difference between the control group and benign group (P < 0.01); the ADC value of the benign group was lower than that of the control group and higher than that of the malignant group (P < 0.01). There was no significant difference between D value and ADC value in the control group. There was no significant difference between D value and ADC value in the benign group; the D value was significantly lower than the ADC value of the malignant group.

The ROC curve for differentiating malignant breast mass-like lesions (migration and movement of breast cancer cells) was analyzed by using various DWI parameters. The area under the curve of D value (AUC) was 0.95, and the sensitivity and specificity of diagnosis were 88.5% and 81.2% when the threshold value was $D \leq 1.06 \times 10^{-3} \text{ mm}^2 / \text{s}$; the sensitivity and specificity of diagnosis were 73.1% and 54.2% when the AU Cof F-value was 0.87 and the threshold value was $f \geq 7.66\%$; when the AUC of ADC was 0.90 and the threshold value was $ADC \leq 1.15 \times 10^{-3} \text{ mm}^2 / \text{s}$, the diagnostic sensitivity and specificity were 96.0% and 83.3%, respectively, as shown in Figure 2. That was, D value has high diagnostic efficiency, followed by ADC value, f value and D* value.

Study on Migration and Movement of Hepatocellular Carcinoma Cells Based on Intravoxel Incoherent Motion Imaging

Table 2 is a comparison of the parameters of hepatic hemangioma and malignant hepatic lesions. Figures 3 and 4 are the results of migration and movement of hepatocellular carcinoma cells in 46-year-old patients with hepatic hemangioma and 51-year-old patients.

According to Table 2, the ADC, D and f values of hepatic hemangioma were higher than those of malignant hepatic lesions, and the difference was statistically significant (P < 0.05); the difference of D* value was not statistically significant (P = 0.499).

The diagnostic efficacy of the parameters of the IVIM bi-index model for hepatic malignant lesions is shown

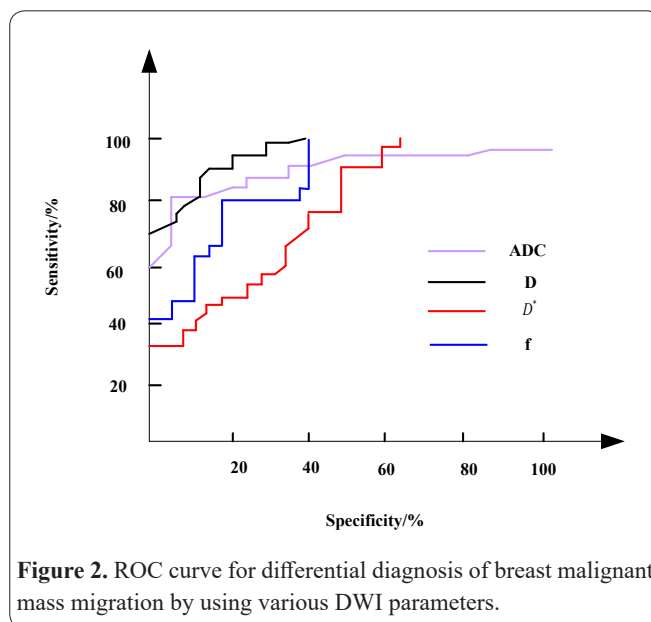


Figure 2. ROC curve for differential diagnosis of breast malignant mass migration by using various DWI parameters.

Table 2. Comparison of parameters of hepatic hemangioma and malignant hepatic lesions.

The nature of lesions	ADC ($\times 10^{-3}$ mm ² /s)	D ($\times 10^{-3}$ mm ² /s)	D* ($\times 10^{-3}$ mm ² /s)	F
Hepatic hemangioma	1.42(0.68)	1.17(0.83)	64.53(74.79)	0.35(0.24)
Malignant lesions of the liver	1.10(0.28)	0.76(0.42)	46.83(53.44)	0.27(0.15)
F value	-3.846	-2.728	-0.677	-2.068
P value	<0.001	0.006	0.499	0.039

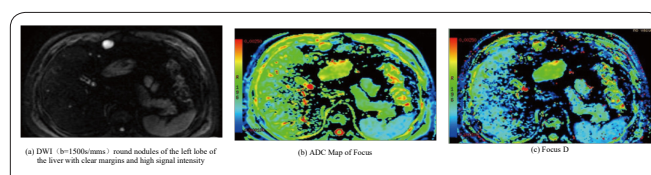


Figure 3. A 46-year-old patient with hepatic hemangioma.

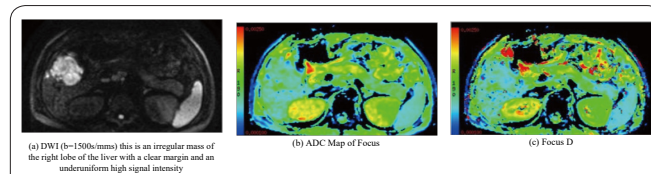


Figure 4. A 51-year-old patient with moderately to poorly differentiated HCC.

in Tables 3 and 4. The best thresholds of ADC, D and fare 1.31, $0.79 \times 10^{-3} \text{ mm}^2 / \text{s}$ and 0.346; the sensitivity and specificity of diagnosing malignant liver lesions were 76.48% and 79.56%, 88.25% and 52.28%, 52.93% and 79.54%, respectively. The AUCs of the three groups were 0.820, 0.727 and 0.672 (all P < 0.05), and there was no significant difference in the pairwise comparison. There was a significant difference between the ADC

Table 3. The diagnostic efficacy of the IVIM dual index model for malignant liver lesions.

Parameter	ADC ($\times 10^{-3} \text{ mm}^2/\text{s}$)	D ($\times 10^{-3} \text{ mm}^2/\text{s}$)	D* ($\times 10^{-3} \text{ mm}^2/\text{s}$)	F
Threshold	1.31	0.79	63.86	0.346
AUC (95% CI)	0.820(0.712,0.929)	0.727(0.584,0.868)	0.556(0.389,0.725)	0.672(0.526,0.819)
P value	<0.001	0.007	0.498	0.038
Sensitivity (%)	76.48	88.25	52.93	52.93
Specificity (%)	79.56	52.28	68.19	79.54

Table 4. Parameters of different types of solid liver lesions.

Parameter	ADC ($\times 10^{-3} \text{ mm}^2/\text{s}$)	D ($\times 10^{-3} \text{ mm}^2/\text{s}$)	D* ($\times 10^{-3} \text{ mm}^2/\text{s}$)	F
Hepatic hemangioma	1.42 (0.68)	1.17(0.85)	64.53(74.79)	0.35(0.24)
HCC	1.07 (0.29)	0.81(0.37)	48.77(60.87)	0.26(0.14)
ICC	1.17 (0.21)	0.70(0.44)	4.07(2.43)	0.37(0.19)
Hepatic metastases	1.29 (1.97)	0.73(1.64)	32.25(70.03)	0.31(0.39)
χ^2	18.534	8.568	1.607	7.597
P value	<0.001	0.037	0.659	0.056

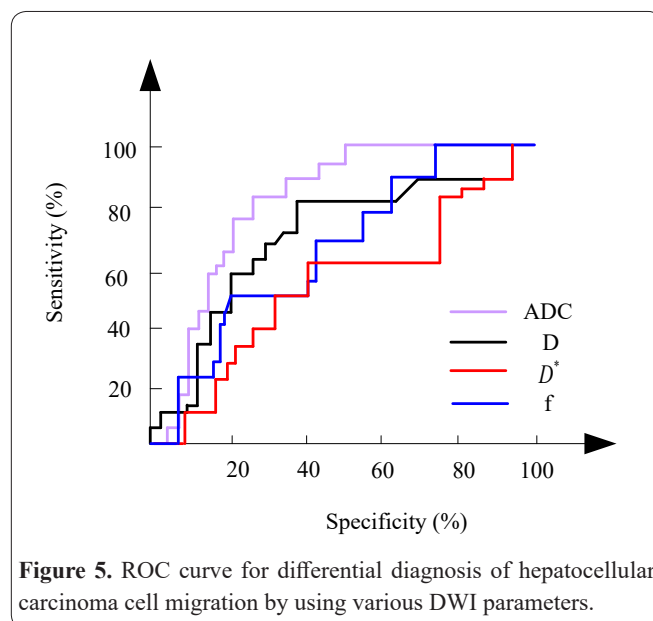
value ($\chi^2 = 18.553$, $P < 0.01$) and D value ($\chi^2 = 8.569$, $P = 0.036$) of four types of FHL. There was no significant difference in the other parameters, shown in Table 4.

Discussion

At present, DWI was the only imaging method that can observe the micro-movement of water molecules *in vivo*. The diffusion limitation caused by the increase of local cell density in breast cancer patients exceeds the perfusion increase caused by the increase of local microvessel density in breast cancer patients, so the ADC value decreases, which is the basis of ADC value used to differentiate benign and malignant breast lesions. In clinical work, due to the differences in MR machine type, scanning parameters and b value, there were great differences in the reports about the diagnostic value of DWI in breast benign and malignant lesions. Because of the irregular arrangement of the capillary network in biological tissue and the irregular movement of blood in microcirculation like water molecules, the micro-movement of water molecules in each pixel includes the diffusion of water molecules driven by simple temperature and the movement of tissue microcirculation. Therefore, the ADC value contains both diffusion and perfusion information.

Normal breast tissue has fewer blood vessels and lower blood perfusion (23). Most of the enhancement scans show scattered slight enhancement. In this study, the f value of the control group was $(4.82 \pm 1.08)\%$, suggesting that normal breast tissue is a low perfusion organ. Therefore, its DWI signal attenuates exponentially with the change of b value. Breast cancer cell proliferation was vigorous, cell density was high, extracellular volume was reduced, at the same time, the limitation of cell biofilm and the adsorption of macromolecular substances (such as protein) on water molecules were enhanced, and there are more immature tumor blood vessels that cause the perfusion fraction to increase, both of them make DWI signal show double exponential decay in the opposite way.

In this study, the diffusion and perfusion information of DWI were separated by IVIM bi-index model

**Figure 5.** ROC curve for differential diagnosis of hepatocellular carcinoma cell migration by using various DWI parameters.

technology, which makes the true diffusion reflecting the change of cell density more accurate. The results show that the D value and ADC values of the malignant group were significantly lower than those of the benign group and control group. There was no significant difference between the D value and ADC values of the control group and the benign group. It may be related to the cell density of malignant mass higher than that of benign mass and normal breast tissue, and the effect of local microcirculation perfusion on diffusion was less. However, the D value of the malignant group was significantly lower than that of ADC value, suggesting that although the cell density was higher. The effect of degree on diffusion counteracts the perfusion caused by the increase of local microvessel, but the effect of microcirculation perfusion on diffusion makes D value lower than ADC value. The ROC curve analysis indicates that AUC was 0.95 when D value was used to diagnose malignant breast mass-like lesions. It suggested that there was higher accuracy and the diagnostic sensitivity and specificity were 88.5% and 81.2% when the threshold value was $D \leq 1.06 \times 10^{-3} \text{ mm}^2/\text{s}$. The f value of the malignant group was significantly higher than

that of the benign group and control group, which was related to the increase of immature tumor blood vessels in malignant breast mass and the increase of perfusion. AUC of F-value was 0.87, which indicates that f value has a certain value in the diagnosis of malignant breast mass-like lesions. When the threshold value was $f \geq 7.66\%$, the sensitivity and specificity of diagnosis were 83.3% and 80.8%. D^* reflects the irrelevant movement of blood in the microvascular structure, and has a certain correlation with the average capillary length and blood flow velocity. The value of D^* in malignant group was significantly lower than that in the benign group and control group. It may be due to the slowdown of blood flow velocity in immature tumors in malignant tumors. The AUC of malignant tumors was 0.75, suggesting that the diagnostic value was medium. The threshold value $D^* \leq 94.72 \times 10^{-3} \text{ mm}^2 / \text{s}$ was 73.1%, and the diagnostic sensitivity and specificity were 54.2%. ROC curve analysis shows that D value has high diagnostic efficiency, followed by ADC value, f value and D^* value.

In this study, four kinds of the most common solid FHL were selected, including benign hepatic hemangioma, malignant HCC, ICC and liver metastases. The results show that the ADC, D and f values of hepatic hemangioma were higher than those of common malignant hepatic lesions, which were basically consistent with previous studies. In the solid components of malignant lesions, the cell density was usually higher, and there were factors such as fibrosis in the tumors, so the diffusion of water molecules was usually more restricted, resulting in lower ADC and D values. Hepatic hemangioma was rich in blood sinuses and blood supply, and the perfusion effect accounts for a large proportion, and f increases; while in malignant lesions, there were many new microvessels, but the development was incomplete, slender and distorted, resulting in F lower than that of hepatic hemangioma. ROC curve analysis showed that there was no significant difference in AUC values of ADC, D and f between benign and malignant FHL in the differential diagnosis of migration and movement of hepatocellular carcinoma cells.

Imaging has many applications in biological research (24-33). Imaging is used in angiogenesis of ovarian tumors (34), breast cancer (35), nasopharyngeal carcinoma (36), prostate cancer (37, 38), dosimetry purpose (39, 40) and tumor research (41).

It has even recently been found to be used in chest high-resolution computed tomography imaging findings of coronavirus disease 2019 (Covid-19) pneumonia (42). Cancer research has yielded good results through the study of gene expression as well as biotechnological methods (43-48).

According to the IVIM bi-index model, a series of b values from low to high was applied to reflect the characteristics of diffusion and perfusion of normal breast tissue, benign and malignant breast masses. Through quantitative analysis of various parameters related to diffusion and perfusion, new viewpoints and perspectives were provided for identifying the movement patterns of benign and malignant breast lesions. This study confirms that the D value, D^* value and f value of perfusion and diffusion related index provided by the IVIM bi-index model have certain value in the diagnosis of breast mass-like lesions. Among

them, the D value has the highest diagnostic efficiency. Whether D value can be used as an independent index of differential diagnosis needs further analysis of large sample data.

For the study of migration and movement of hepatocellular carcinoma cells, only hepatic hemangioma, abscess, focal nodular hyperplasia and adenoma were included in the benign lesions. The blood supply status of the lesions was not analyzed. The difference in blood supply may significantly affect the v and f values, and the repeatability of parameters measurement of the IVIM bi-index model was not studied. IVIM bi-index model can provide more accurate water molecular diffusion and microcirculation perfusion information, but it has limited value in diagnosis and differential diagnosis of common solid FHL. The diagnostic efficiency of the ADC value was higher, which may be due to the small sample size. It is necessary to increase the sample size for further study.

References

1. Yan C, Xu J, Xiong W, Wei Q, Feng R, Wu Y, Liu Q, Li C, Chan Q, Xu Y. Use of intravoxel incoherent motion diffusion-weighted MR imaging for assessment of treatment response to invasive fungal infection in the lung. *Eur Radiol* 2017; 27(1):212-21.
2. Meeus E, Novak J, Withey S. Evaluation of intravoxel incoherent motion fitting methods in low-perfused tissue. *J Magn Reson Imaging* 2017; 45: 1325-1334.
3. Yan N. Resisting power attacks scheme based on signed integer splitting form. *J Chin Acad Electron Inf Technol* 2017; 12: 438-442.
4. Rong D, Mao Y, Hu W. Intravoxel incoherent motion magnetic resonance imaging for differentiating metastatic and non-metastatic lymph nodes in pancreatic ductal adenocarcinoma. *Eur Radiol* 2018; 28: 2781-2789.
5. Sun L, Zhang Y, Chen X. Repetitive-control-based control technology for microgrid inverters. *J Power Supply* 2018; 16: 38-44.
6. Zhang C, Wong S, Uiterwijk R. Intravoxel incoherent motion imaging in small vessel disease. *Stroke*, 2017; 48: 658-663.
7. Zhang X, Lang Y. Power management and implementation based on ethernet switch. *Chin J Power Sources* 2017; 41: 630-632.
8. Liu Y, Li H, Zhang J.. Potassium iodate differently regulates the proliferation, migration, and invasion of human thyroid cancer cells via modulating mir-146a. *Cancer Invest* 2017; 35: 122-128.
9. Hu Y. Main problems and solutions of mechanical and electrical equipment installation in intelligent building branch project. *Autom Instrum* 2017; 4: 159-161.
10. Woo S, Suh C Kim, S. Magnetic resonance imaging for detection of parametrial invasion in cervical cancer: An updated systematic review and meta-analysis of the literature between 2012 and 2016. *European Radiology*, 28: 1-12.
11. Lin, W.X., 2017. Oscillation analysis for a class of even order neutral differential equations with damping terms. *J Jilin Univ (Science Edition)*, 2017; 55: 1073-1076.
12. Sun Y, Xiao Q, Hu F. Diffusion kurtosis imaging in the characterization of rectal cancer: utilizing the most repeatable region-of-interest strategy for diffusion parameters on a 3T scanner. *Eur Radiol* 2018; 28: 1-10.
13. Ding S. Accurate evaluation and simulation of load carrying risk of building bearing column. *Comput Simul* 2018; 35: 349-352.
14. Zhou Y, Xu Q, Shang J. Crocin inhibits the migration, invasion, and epithelial-mesenchymal transition of gastric cancer cells via miR-320/KLF5/HIF-1 α signaling. *J Cell Physiol* 2019; 234: 17876-17885.

15. Godbole M, Tiwary K, Badwe R. Progesterone suppresses the invasion and migration of breast cancer cells irrespective of their progesterone receptor status - a short report. *Cell Oncol* 2017; 40: 411-417.
16. Niu J, Li W, Wang H. Intravoxel incoherent motion diffusion-weighted imaging of bone marrow in patients with acute myeloid leukemia: a pilot study of prognostic value. *J Magn Reson Imaging* 2017; 46: 476-482.
17. Zhang C, Wong S, Uiterwijk R. Intravoxel incoherent motion imaging in small vessel disease: microstructural integrity and microvascular perfusion related to cognition. *Stroke* 2017; 48: 658-663.
18. Gao Q, Lu S, Xu X. Quantitative assessment of hyperacute cerebral infarction with intravoxel incoherent motion MR imaging: Initial experience in a canine stroke model. *J Magn Reson Imaging* 2017; 46: 550-556.
19. Wengler K, Fukuda T, Tank D. Intravoxel incoherent motion (IVIM) imaging in human achilles tendon. *J Magn Reson Imaging* 2018; 48: 1690-1699.
20. Li X, Wang P, Li D. Intravoxel incoherent motion MR imaging of early cervical carcinoma: correlation between imaging parameters and tumor-stroma ratio. *Eur Radiol* 2017; 28: 1-9.
21. Peng WX, Wang LS, Mirzaee M, Ahmadi H, Esfahani MJ, Fremaux S. Hydrogen and syngas production by catalytic biomass gasification. *Energy Convers Manag* 2017; 135:270-3.
22. Peng WX, Ge SB, Ebadi AG, Hisoriev H, Esfahani MJ. Syngas production by catalytic co-gasification of coal-biomass blends in a circulating fluidized bed gasifier. *J Clean Prod* 2017; 168:1513-7.
23. Peng W, Lin Z, Wang L, Chang J, Gu F, Zhu X. Molecular characteristics of *Illicium verum* extractives to activate acquired immune response. *Saudi J Biol Sci* 2016; 23(3): 348-52.
24. Liang X, Shi W, Wang X, Qin J, Wang L, Wu X, et al. Brainstem schwannoma: A case report and review of clinical and imaging features. *Int J Radiat Res.* 2020; 18 (3) :605-610
25. Tayeri H, Sattarzadeh Khameneh E, Zolghadri S, Kakaei S, Sardari D. Optimized production, quality control and biological assessment of ⁶⁸Ga-bleomycin as a possible PET imaging agent. *Int J Radiat Res.* 2020; 18 (2) :235-241.
26. Ahmadi N, Karimian A, Nasrabadi M, Rahmim A. Assessment of fetal and maternal radiation absorbed dose in ¹⁸F-FDG PET imaging. *Int J Radiat Res.* 2019; 17 (4) :651-657.
27. Salimi Y, Deevband M, Ghafarian P, Ay M. Uncertainties in effective dose estimation for CT transmission scan in total body PET-CT imaging with Auto mA3D tube current modulation . *Int J Radiat Res.* 2018; 16 (4) :465-472.
28. Abtahi S, Jafari Khalilabadi R, Aftabi S. An investigation into the effect of magnetic resonance imaging (MRI) echo time spacing and number of echoes on the sensitivity and dose resolution of PAGATUG polymer-gel dosimeter. *Int J Radiat Res.* 2017; 15 (2) :185-196.
29. Heck K, Korkusuz Y, Happel C, Grünwald F, Korkusuz H. Percutaneous microwave ablation of thyroid nodules: efficacy evaluation with ^{99m}Tc - pertechnetate and ^{99m}Tc-MIBI functional imaging. *Int J Radiat Res.* 2016; 14 (2) :91-98.
30. Salihin Yusoff M, Zakaria A. Determination of the optimum filter for qualitative and quantitative ^{99m}Tc myocardial SPECT imaging. *Int J Radiat Res.* 2009; 6 (4) :173-182.
31. Jalilian A, Mirazizi F, Nazem H, Garousi J, Bolourinovin F, Sa-deghpour H. Preparation and quality control of radiolabeled streptokinase for Thrombosis imaging. *Int J Radiat Res.* 2009; 6 (4) :195-200.
32. Azadbakht B, Zahmatkesh M, Hadad K, Bagheri S. Verification of the PAGAT polymer gel dosimeter by photon beams using magnetic resonance imaging. *Int J Radiat Res.* 2008; 6 (2) :83-87.
33. Khosravi H, Sarkar S, Takavar A, Saghari M, Shahriari M. Planar and SPECT Monte Carlo acceleration using a variance reduction technique in I131 imaging. *Int J Radiat Res.* 2007; 4 (4) :175-182.
34. Liu X, Shen C. Correlation of ultrasound perfusion imaging and angiogenesis of ovarian tumors. *Int J Radiat Res.* 2019; 17 (4) :559-567.
35. Choi J, Rim C, Kim Y, Yang D. Cumulative radiation exposure dose of diagnostic imaging studies in breast cancer patients. *Int J Radiat Res.* 2019; 17 (2) :275-281.
36. Chen H, Huang H, Li G, Huang D, Huang S, Wang Z. Application of computed tomography and magnetic resonance imaging fusion images for delineating gross tumor volume in three-dimensional conformal radiotherapy of nasopharyngeal carcinoma. *Int J Radiat Res.* 2017; 15 (3) :251-257.
37. Mahdavi S R, Jazayeri Gharehbagh E, Mofid B, Jafari A H, Nikoofar A R. Accuracy of the dose delivery in prostate cancer patients-using an electronic portal imaging device (EPID) . *Int J Radiat Res.* 2017; 15 (1) :39-47.
38. Robotjazi M, Mahdavi S, Nikofar A, Bolouri B, Baghani H. Optimization of clinical target volume delineation using magnetic resonance spectroscopic imaging (MRSI) in 3D conformal radiotherapy of prostate cancer. *Int J Radiat Res.* 2014; 12 (4) :303-309.
39. Jomehzadeh A, Shokrani P, Mohammadi M, Amouheidari A. A quality assurance program for an amorphous silicon electronic portal imaging device using in-house developed phantoms: a method development for dosimetry purposes . *Int J Radiat Res.* 2014; 12 (3) :257-264.
40. Teimoori Sichani M, Amoui M, Akhlaghpour S, Hosntalab M. Quantitative SPECT and planar ³²P bremsstrahlung imaging for dosimetry purpose –An experimental phantom study. *Int J Radiat Res.* 2014; 12 (2) :129-138.
41. Jalilian AR, Fateh B, Ghergherehchi M, Karimian A, Matlloobi M. Preparation, distribution, stability and tumor imaging properties of [⁶²Zn] bleomycin complex in normal and tumor-bearing mice. *Int J Radiat Res.* 2003; 1 (1) :37-44.
42. He X, Zheng J, Ren J, Zheng G, Liu L. Chest high-resolution computed tomography imaging findings of coronavirus disease 2019 (Covid-19) pneumonia. *Int J Radiat Res.* 2020; 18 (2) :343-349.
43. Falahatgar D, Farajnia S, Zarghami N, Tanomand A, Khosroshahi SA, Akbari B, Farajnia H. Expression and Evaluation of HuscFv Antibody -PE40 Immunotoxin for Target Therapy of EGFR-Overexpressing Cancers. *Iran J Biotechnol.* 2018; 16(4): e1743.
44. Avand A, Akbari V, Shafizadegan S. In Vitro Cytotoxic Activity of a *Lactococcus lactis* Antimicrobial Peptide Against Breast Cancer Cells. *Iran J Biotechnol.* 2018; 16(3): e1867.
45. Bahadori M, Baharara J, Amini E. Anticancer Properties of Chrysin on Colon Cancer Cells, In vitro and In vivo with Modulation of Caspase-3, -9, Bax and Sall4. *Iran J Biotechnol.* 2016; 14(3): 177-184.
46. Behfarjam F, Rostamzadeh J, Zarei MA, Nikkhoo B. Association of Two Polymorphic Codons in P53 and ABCC1 Promoter with Prostate Cancer. *Iran J Biotechnol.* 2015; 13(1): 49-54.
47. Bordbar M, Darvishzadeh R, Pazhouhandeh M, Kahrizi D. An overview of genome editing methods based on endonucleases. *Mod Genet J* 2020; 15(2): 75-92.
48. Jamalzadeh L, Ghafoori H, Aghamaali M, Sariri R. Induction of Apoptosis in Human Breast Cancer MCF-7 Cells by a Semi-Synthetic Derivative of Artemisinin: A Caspase-Related Mechanism. *Iran J Biotechnol.* 2017; 15(3): 157-165.